Method for using spectral flow data to predict vortex-induced vibration onset of static structures

Kevin R. Moore[1], Hannah K. Ross[2], Kirk L, Bonney[1], and Brent J. Summerville[2]

[1]Sandia National Laboratories *, PO Box 5800 MS 0717 Albuquerque, NM 87185, USA
[2]National Laboratory of the Rockies, 15013 Denver West Parkway, Golden, CO 80401, USA

Correspondence: Kevin R. Moore (kevmoor@sandia.gov)

Abstract. Spectral representations of vortex shedding behavior, such as airfoil data derived from computational fluid dynamics or experiment, can support the efficient identification of potential vortex-induced vibration onset. However, use of such data is hindered by the myriad of practical considerations required to scale, filter, and rank the risk of overlap between natural frequencies and shedding frequencies. This problem spans across Reynolds number, local angle of attack, and local skew angle, in addition to frequency harmonics, interpolation, and multi-body multi-element structures. The combinatorial scale of the problem additionally necessitates efficient numerical methods. This paper presents a reproducible, open-source framework with accompanying source code and a graphical user interface. With the improvements here, these problems can be addressed to enable the straightforward use of existing spectral datasets for arbitrary beam-type structures. We describe the methods, present a simple verification case, and exercise the method on a sample structure using a spectral airfoil dataset. The framework enables designers to readily navigate the complex space to identify, avoid, and include (via one-way coupling) the onset of vortex-induced vibration in their design workflows. Code, example datasets, and reproduction assets are openly released.

1 Introduction

Static structures such as communication towers, cables, parked wind turbines, and marine structures can experience vortex-induced vibration. When flow separates periodically in a ~~fluid~~ wake, alternating vortices impose fluctuating forces. If the shedding frequency coincides with a natural structural frequency, large-amplitude oscillations can result. While vortex shedding from cylinders is well characterized (Roshko, 1961; Schewe, 1983), ~~shedding from~~ shapes between a cylinder and a flat plate, such as airfoils, contain~~s~~more complex spectral forcing harmonics~~, which complicates use for design . This can be especially important for certain types of wind energy structures, including~~ . This complicates their use in design and is relevant to vertical-axis wind turbines (Sakib and Griffith, 2022) ~~,~~and large horizontal-axis wind turbines (Grinderslev et al., 2023)~~.~~ ~~These structures leverage airfoils that produce bluff-body shedding in some regimes~~, where parked or highly yawed airfoils can behave as bluff bodies.

*Sandia National Laboratories is a multimission laboratory managed and operated by National Technology and Engineering Solutions of Sandia, LLC., a wholly owned subsidiary of Honeywell International, Inc., for the U.S. Department of Energy's National Nuclear Security Administration under contract DE-NA-0003525

For airfoils, Sheldahl and Klimas (1981) compiled polar data for symmetric NACA sections up to an angle of attack (AoA) of 180°. At high AoAs, this dataset approached flat-plate behavior. Unsteady pressure measurements by Swalwell et al. (2003) on a NACA 0021 demonstrated multiple distinct vortex shedding peaks that decreased in frequency with AoA, whereas Strouhal numbers based on projected chord remained nearly constant and consistent with flat-plate behavior, like that characterized by Chen and Fang (1996). More recently, Benner et al. (2019) conducted an experimental campaign using the NACA 0021 in water and observed significant energy across multiple Strouhal harmonics depending on AoA, but the results were generally consistent with prior work.

Modern computational studies have extended this kind of study to other airfoils. Bidadi et al. (2024) performed three-dimensional improved delayed detached-eddy simulations of FFA-W3 airfoils over the full 0–360° AoA range ~~. They showed Strouhal numbers collapse to nearly flat-plate behavior for high AoAs but for a continuum of airfoil thickness between a flat plate and cylinder. However, for low AoAs , or near 180~~at $Re = 10^7$. They reported a Strouhal number of about 0.15 for slender airfoils in separated high-AoA conditions, but the response varies with airfoil thickness and incidence. Low AoAs and near-180° ~~, there is greater variation. Further investigation into this dataset also~~ reversed-flow cases show greater variation, and further investigation into these datasets shows multiple frequency peaks for many conditions~~and confirms complexities~~ , consistent with the regime multiplicity identified by Fernandez-Aldama et al. (2025).

~~There is now a significant body of information suggesting that 1) vortex shedding of airfoils generally follows flat-plate behavior, 2) Reynolds effects may be minimal for non-transition conditions at high angles, 3) there is a continuum of Strouhal numbers between a flat plate (lower) and cylinder (higher) based on thickness, and 4) there is some variance in Strouhal numbers with AoA at high AoAs, and significant variance in Strouhal numbers at low AoAs.~~ The relevant Reynolds-number regime is therefore stated with the Strouhal data. For example, the inclined-flat-plate measurements of Chen and Fang (1996) covered $Re = 3.5 \times 10^3$ to 3.2×10^4 and found little Reynolds-number dependence for fully separated flow between 10° and 90° incidence, whereas Swalwell et al. (2003) measured a stalled NACA 0021 at $Re = 2.70 \times 10^5$ and Bidadi et al. (2024) simulated wind-turbine airfoils at $Re = 10^7$. The classical circular-cylinder value near $St = 0.2$ is useful for first-pass screening, but it should not be treated as a universal value for an airfoil or for a different Reynolds-number regime. With this knowledge, the next step is to develop a practical process, spanning the highly dimensional problem, that uses ~~the~~ source data for design with greater precision.

1.1 Objectives

While this topic is relevant to a broad variety of applications, for this paper, we ~~will~~ focus on the example case of a small, vertical-axis distributed wind turbine. The case is chosen because this structure has a clear overlap potential between shedding frequency and structural natural frequency. For the reference turbine described in Moore et al. (2024), the first three major blade-strut system natural frequencies are approximately 1.8, 4.5, and 5.7 Hz. ~~A cylinder's Strouhal number just below the~~ Using the first-pass circular-cylinder estimate $St \approx 0.2$ near the 4.5 m/s cut-in inflow velocity ~~at 4.5 ms^{-1} is approximately 0.2~~ (Roshko, 1961), and ~~for a flat plate it ranges between 0.2 and 0.8~~ flat-plate values that can range much higher depending on AoA (Chen and Fang, 1996)~~. This~~ , this simplified analysis puts the shedding frequency range between 1.8 Hz and 7.2 Hz~~, or~~

directly on top of . That range directly overlaps the blade natural frequencies for certain parked angles and low-velocity inflow conditions.

Failing to design around the potential shedding overlap or to account for the additional fatigue cycles poses a significant risk to this type of structure or other structures with similar properties. Additionally, these types of shapes do not produce only a single shedding frequencyin the wake, and vibration can lock into different harmonics Airfoil wakes can contain multiple shedding frequencies. Separately, at a given oscillation frequency, multiple limit-cycle amplitudes can be reached depending on initial conditions (Grinderslev et al., 2022). Sensitivities in forced-motion VIV simulations were investigated by Grinderslev et al. (2023). Prior work (Bidadi et al., 2024; VimalKumar et al., 2024) has effectively shown how to apply the dominant frequency to highlight one problem area, but there are other risks not covered by this initial breakthrough work. These risks include 1) the effect of the drag vector's frequency content, 2) built-up structures' range of AoAs for a given inflow condition, 3) modal harmonics, 4) non-primary shedding frequency impacts, and 5) how to reliably traverse sparse data through interpolation. These are the main contributions this paper aims to make.

1.2 Paper structure

The paper is organized as follows: Sect. 2 describes the methods used, including spectral data decomposition, linear algebra to resolve multi-body AoAs, interpolation in both Reynolds and Strouhal domains, and combinatorial reduction. Sect. 3 introduces the VorLap code and graphical interface. Sect. 4 gives a simplified verification exercise, and Sect. 5 demonstrates the framework on a reference structure. Sect. 6 closes by identifying next steps.

2 Methods

The workflow produces two complementary outputs: (i) a frequency-overlap screening metric to identify potential vortex-shedding alignment with structural modes, and (ii) reconstructed time-domain force signals for one-way coupling into structural solvers. The reconstruction is needed because frequency proximity alone does not provide phase information or time histories for synthesizing net loads across multiple components and nodes.

2.1 Spectral data decomposition

Spectral data can come from various sources, including experiments, computational fluid dynamics, and lower-fidelity methods. Regardless of the source, the objective is to reduce the time series into a non-dimensional spectral form that can be scaled and used for other flow conditions. The primary non-dimensional number of interest is the Strouhal number, defined in Eq. (1), with the frequency in hertz as f, the inflow velocity in meters per second as ~~V_{int}~~V_∞, and the characteristic length in meters as ~~L~~c_n, the flow-normal projected chord or major axis. Once a frequency is non-dimensionalized by Strouhal number, it can then be scaled for different characteristic lengths and inflow velocities. We reserve L for lift.

$$St = \frac{fL}{V_{\text{inf}}}$$

$$St = \frac{fc_n}{V_\infty} \tag{1}$$

For non-circular shapes, the characteristic length c_n is taken as the flow-normal projection of the major axis. Though we do not discuss it in detail, this characteristic length was chosen over the total planform projection (including thickness of the secondary axis), as it produced less variation in Strouhal number across wide AoAs.

We also define the chord Reynolds number using the physical chord length c, freestream density ρ, and dynamic viscosity μ,

$$Re_c = \frac{\rho V_\infty c}{\mu}. \tag{2}$$

Additionally, we define the lift and drag coefficients, which are necessary to scale the force amplitudes independent of the Strouhal frequency scaling. These are defined in Eq. (3) and Eq. (4), with the lift L, drag D, fluid density ρ, planform area S (typically chord times unit length), and freestream velocity ~~V_{inf}~~V_∞.

$$C_L = \frac{L}{0.5\rho S V_{\text{inf}}^2}$$

$$C_L = \frac{L}{0.5\rho S V_\infty^2} \tag{3}$$

$$C_D = \frac{D}{0.5\rho S V_{\text{inf}}^2}$$

$$C_D = \frac{D}{0.5\rho S V_\infty^2} \tag{4}$$

Next, in order to move from the time domain to the frequency domain, we ~~can conduct a~~ compute the nonredundant one-sided coefficients of the standard discrete Fourier transform ~~like that~~ as shown in Eq. (5). In this transform, X_k is the complex ~~frequency domain coefficient, with the real part as the amplitude (properly scaled in Eq. (6), accounting for negative frequencies), and the imaginary as the phase. Then,~~ frequency-domain coefficient, x_n is the time-domain sample data, and N is the total number of samples. ~~It should be noted that the mean of the signal is included as the k=0 position, and is reconstructed likewise in this single-sided real-value analysis.~~ For clarity, Eqs. (5), (6), (9) and (10) assume even N. The one-sided peak amplitude retained for each positive-frequency bin is denoted by A_k and is computed from the magnitude of X_k as shown in Eq. (6). The corresponding phase angle is $\phi_k = \arg(X_k)$. The signed mean is retained as $A_0 = X_0/N$, and the Nyquist bin $k = N/2$ is retained without the factor of two because it is not paired with a distinct negative-frequency coefficient. For odd N, the upper one-sided index is $\lfloor N/2 \rfloor$ and every positive-frequency bin is doubled. For PSD ranking, the mean is removed before computing the PSD so the zero-frequency component does not dominate the peak ordering, while A_0 is retained separately for reconstruction.

$$X_k = \sum_{n=0}^{N-1} x_n \, e^{-i\frac{2\pi}{N}kn}, \quad k = 0, 1, 2, \ldots, N/2 \tag{5}$$

$$A_k = \frac{2|X_k|}{N}$$

$$A_k = \begin{cases} \dfrac{X_0}{N}, & k = 0, \\ \dfrac{2|X_k|}{N}, & k = 1, 2, \ldots, N/2 - 1, \\ \dfrac{|X_{N/2}|}{N}, & k = N/2 \end{cases} \tag{6}$$

$$\phi_k = \arg(X_k) \tag{7}$$

Equation (8) is the frequency vector corresponding to the X_k coefficients, with the frequency f_k in hertz, and the sampling frequency (inverse of the time step) f_s.

$$f_k = \frac{k}{N} f_s, \quad k = 0, 1, 2, \ldots, N/2 \tag{8}$$

Equation (9) is the inverse of Eq. (5) ~~(written using the cosine notationas opposed to the complex exponent)~~written using cosine notation, which can be used to reconstruct a real-valued signal after the amplitudes and frequencies are scaled.

$$x_n = \frac{1}{N}\sum_{k=0}^{N-1} |X_k| \cos\left(\frac{2\pi k n}{N} + \phi_k\right), \quad k = 0, 1, 2, \ldots, N/2$$

$$x_n = A_0 + \sum_{k=1}^{N/2} A_k \cos\left(\frac{2\pi k n}{N} + \phi_k\right), \quad n = 0, 1, 2, \ldots, N-1 \tag{9}$$

However, since we are interested in identifying the major shedding frequencies, a reliable way to sort the transform is needed. Sorting by amplitude alone provides mixed results, while sorting by power spectral density (PSD) clearly differentiates between areas of high energy content.

$$PSD_k = \begin{cases} \dfrac{1}{N f_s}|X_k|^2, & k = 0 \text{ or } k = N/2, \\ \dfrac{2}{N f_s}|X_k|^2, & k = 1, 2, \ldots, N/2 - 1 \end{cases} \tag{10}$$

We use the combined force coefficient

$$C_F = \sqrt{C_L^2 + C_D^2} \tag{11}$$

to rank the dominant peaks: the PSD is computed from the C_F signal after removing its mean, and the peaks are sorted by PSD magnitude. Additionally, due to the size of the problem across a wide range of AoAs, Reynolds numbers, and different shapes, we need a reliable way to reduce the data without sacrificing accuracy. Keeping only the first several hundred ~~sorted frequencies~~ ranked peaks enables a reconstruction of accurate signals with reduced memory.

Putting this ~~frequency space~~ frequency-space analysis into practice, Fig. 1 shows a sample lift and drag time signal and PSD frequency plot. The ~~frequency content for the sample~~ NACA 0018 ~~data~~ time histories in Figs. 1 to 3 are preliminary CFD force-history data distributed with the VorLap repository (Sandia National Laboratories, 2026). They are used only as a transparent workflow example to demonstrate the VorLap method, not as a standalone validation dataset. Future work is planned to replace this preliminary example with a high-quality CFD spectral dataset. The frequency content at 164° (16° reversed flow) AoA shows multiple peaks around 0.25 Hz and 1.25 Hz, corresponding to Strouhal numbers of around 0.02 and 0.09 before the illustrative offset discussed below. These numbers are markedly different from the flat-plate experimental values referenced and highlight the importance of ~~this work~~ using application-matched source data for structures that could

experience these conditions.

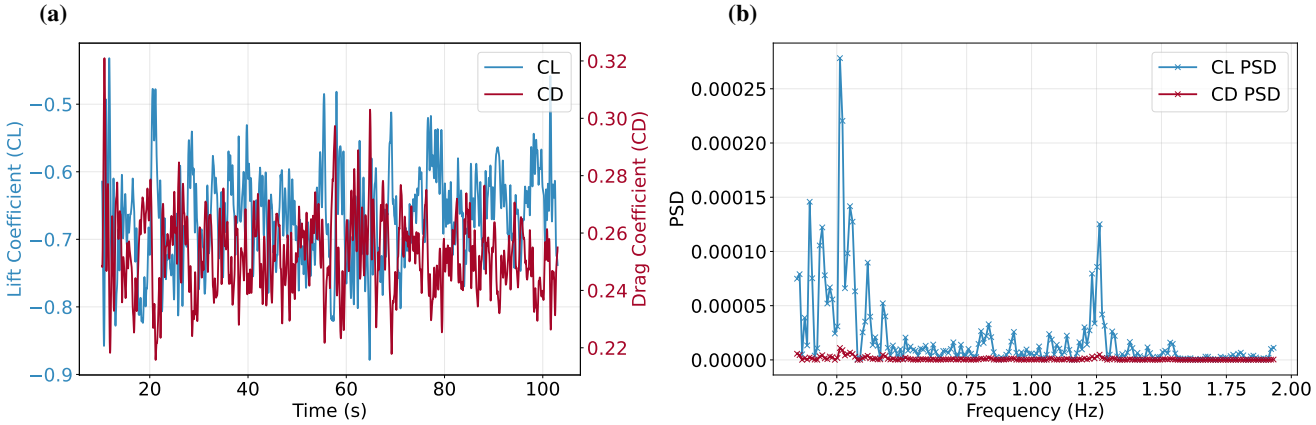


Figure 1. Sample time domain (a) and frequency domain (b) lift and drag data from the preliminary VorLap NACA 0018 CFD example force-history dataset for a 1 m chord ~~NACA 0018~~ airfoil at 164° AoA, an inflow of 3.75 ~~ms^{-1}~~m/s, and ~~a Reynolds number of 5e+05.~~ $Re_c = 5 \times 10^5$ (see Eq. (2)).

The PSD shown in Fig. 1 indicates that the drag has similar frequency content as the lift but at much lower amplitudes. As the AoA approaches 90°, drag dominates, and for some intermediate conditions, different frequency harmonics show up in the lift versus drag. This is illustrated in Fig. 2, which presents the same information as Fig. 1 but for an AoA of 84°. Therefore, the 2-norm of the lift and drag is useful for sorting the peak Strouhal numbers and also enables a reduction of the dataset for computational memory without sacrificing reconstruction accuracy. Additionally, the combined force enables a more efficient overlap identification strategy, as even minor alignment has the potential to excite a modal frequency.

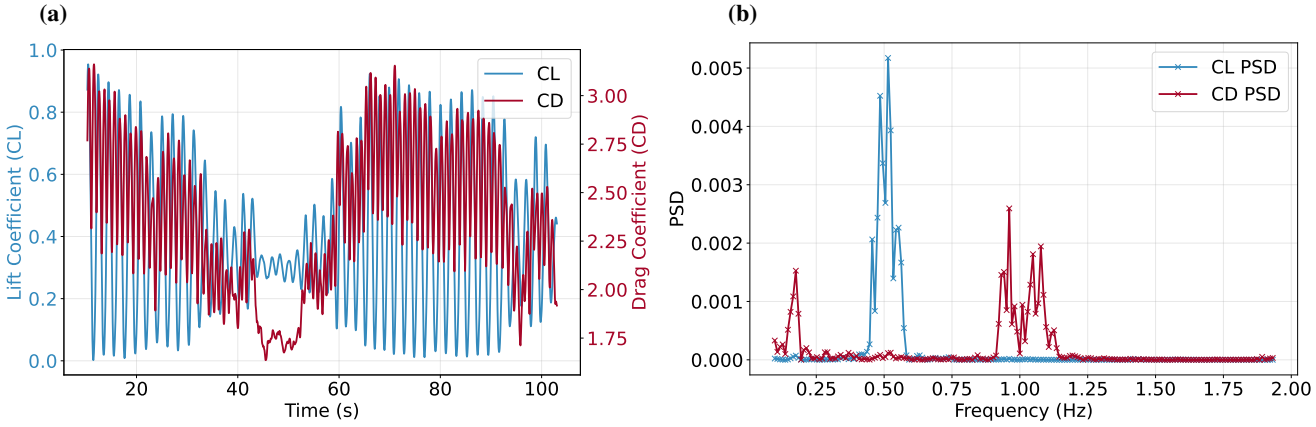


Figure 2. Sample time domain (a) and frequency domain (b) lift and drag data from the preliminary VorLap NACA 0018 CFD example force-history dataset for a 1 m chord ~~NACA 0018~~ airfoil at 84° AoA, an inflow of 3.75 ~~ms^{-1}~~m/s, and ~~a Reynolds number of 5e+05.~~ $Re_c = 5 \times 10^5$ (see Eq. (2)).

By running this analysis for all AoAs (Fig. 3), we can extract ~~all~~ the frequency content, normalize by the Strouhal number, and retain the amplitude and phase information. The figure shows the first 30 ~~frequencies, sorted by the 2-norm of the lift and drag coefficients, termed CF for force coefficient~~ ranked peaks based on the combined force coefficient C_F in Eq. (11). The expected high-AoA Strouhal scale for the comparison datasets is approximately 0.15–0.16: Chen and Fang (1996) report a corrected flat-plate value of about 0.160 for fully separated inclined plates, and Bidadi et al. (2024) report about 0.15 for slender FFA-W3 airfoils in separated high-AoA conditions. The preliminary NACA 0018 example spectra used for Fig. 3 were lower than that range, so a uniform +0.07 offset was applied to the nonzero Strouhal values in this demonstrative dataset to place the dominant high-AoA branch near the published reference scale. This offset is not a universal correction and should be replaced by application-matched spectral data, or treated as a sensitivity parameter, in design use. The offset changes predicted shedding frequencies by $\Delta f = 0.07 V_\infty / c_n$ and therefore shifts overlap bands directly. Future work is planned to generate a higher-quality CFD dataset for this purpose. ~~The multiple harmonics are clearly shown. All frequencies were tuned by increasing the Strouhal number by 0.07 for all Strouhal numbers to better align with other datasets . While accurate airfoil-specific datasets are in progress, the intent of this study is to focus on the methods and impacts for a representative dataset .~~

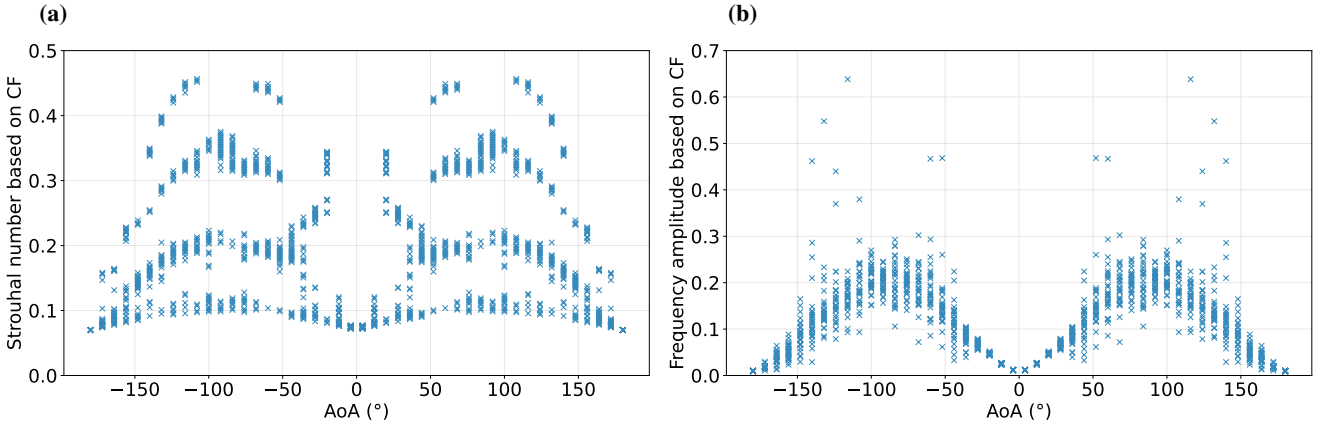


Figure 3. Strouhal number (a) and frequency amplitude (b) for the first 30 ~~sorted frequencies~~ ranked peaks based on $C_F = \sqrt{C_L^2 + C_D^2}$ from the ~~2-norm of the sample lift and drag data~~ preliminary VorLap NACA 0018 CFD example dataset for a 1 m chord ~~NACA 0018~~ airfoil at an inflow of 3.75 ~~ms^{-1}~~ m/s and ~~a Reynolds number of 5e+05. Note that all frequencies were tuned by increasing the~~ $Re_c = 5 \times 10^5$ (see Eq. (2)). The plotted nonzero Strouhal ~~number by~~ values include the uniform +0.07 ~~for all Strouhal numbers~~illustrative offset discussed in the text.

With a complete dataset, we can now use the new geometry and flow conditions with the inverted Strouhal (Eq. (1)), lift coefficient (Eq. (3)), and drag coefficient (Eq. (4)), and with the inverse Fourier transform equation (Eq. (9)) to generate a scaled signal. This process enables independent scaling of both the shedding frequencies and the lift and drag for use in identifying potential shedding-modal frequency overlap, as well as for reconstructing time-domain force signals for one-way coupling.

2.2 Linear algebra for multi-body AoA calculation

To calculate the local AoA and local velocity vector, we use basic linear algebraic rotations and expressions, rotating the inflow vector about the prescribed rotation axis. The inflow velocity vector in the local coordinate frame of each blade element is obtained by rotating the freestream velocity $\mathbf{V}_\infty$ about the rotor axis. In this paper we evaluate parked, quasi-static conditions; rotation is used only to sweep azimuthal orientation and no rotation-induced inflow is added. For rotating cases, a tangential velocity term would be added to form the relative inflow. Specifically, the rotated inflow vector is given by

$$V_{\text{in,rot}} = R(\hat{a}_{\text{rot}}, -\psi_j)\, V_\infty \tag{12}$$

where $\hat{\mathbf{a}}_{\text{rot}}$ is the unit vector defining the rotation axis of the rotor or component, and ψ_j is the azimuthal position angle for index j. The operator $\mathbf{R}(\hat{\mathbf{a}}_{\text{rot}}, -\psi_j)$ denotes a rotation matrix that transforms the global velocity vector into the local frame fixed to the blade element.

Figure 4 provides a pictorial view of the normal and tangential vectors on each multibody component~~, with an example inflow velocity vector in blue and rotation vector in black~~ . The freestream inflow vector and rotation axis are shown in black by the VorLap geometry visualization, with the ~~objective to calculate the~~ rotation axis drawn as a dashed vector. VorLap uses Cartesian global vectors; for this case the inflow direction is $(1, 0, 0)$ and the rotation axis is $(0, 0, 1)$, and these global directions are marked with the small axis triad in the figure. These vectors define the local static AoA and inflow velocity in the blade frame of reference for a given parked state.

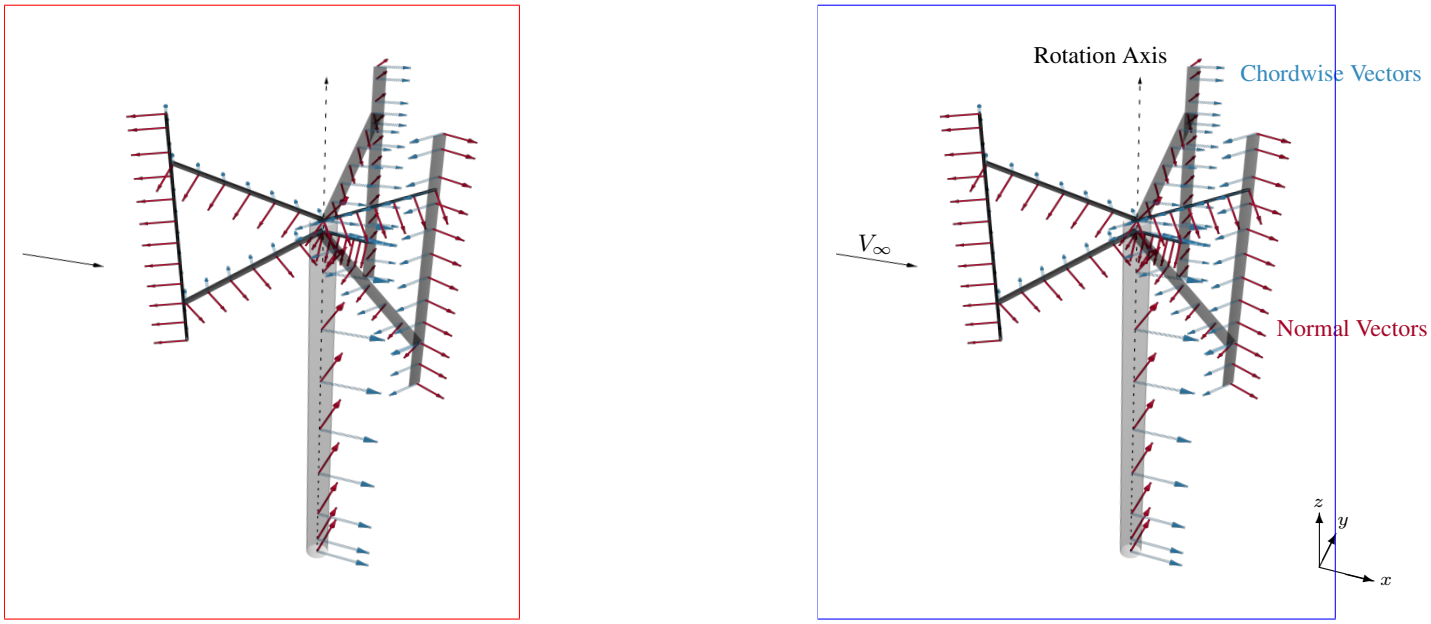


Figure 4. Example ~~built up~~ built-up geometry in semi-transparent grey, with local normal vectors in red, ~~tangential~~ local chordwise vectors in blue, the rotation axis ~~in~~ shown as the dashed black vector, ~~and~~ the freestream inflow vector shown in ~~solid~~ black, and the turbine global axes marked by the black triad in the lower-right corner. ~~This information is~~ The chordwise and normal inflow components (V_c, V_n) used ~~to calculate~~ in Eq. (13)–Eq. (16) are the projections of V_∞ onto the local ~~inflow~~ chordwise and ~~AoAs at every nodal position for all conditions~~normal directions.

At each evaluation point along the blade, the ~~chord direction normalized~~ unit chord vector $\hat{\mathbf{c}}$ and ~~the normal direction~~ unit normal vector $\hat{\mathbf{n}}$ are defined from the local geometry ~~, which is inherent to a given~~ of the multi-body design. ~~Their corresponding unit vectors are representing~~ These vectors represent the local chordwise and normal directions, respectively.

The inflow velocity V components projected onto these directions are then computed as

$$V_c = V_{\text{in,rot}} \cdot \hat{c} \tag{13}$$

$$V_n = V_{\text{in,rot}} \cdot \hat{n} \tag{14}$$

corresponding to the chordwise and normal components of the local inflow velocity.

The local geometric AoA α is defined from these components as

$$\alpha = \tan^{-1}\left(\frac{V_n}{V_c}\right) \tag{15}$$

where the two-argument form of the arctangent is used in implementation to ensure correct quadrant identification.

Finally, the magnitude of the effective local inflow velocity V_{eff} in the two-dimensional chord–normal plane is expressed as

$$V_{\text{eff}} = \sqrt{V_n^2 + V_c^2} \tag{16}$$

This effective speed neglects any spanwise velocity component and represents the local magnitude of the relative flow that governs the aerodynamic lift and drag (including the shed frequency scaling) experienced by the section.

2.3 Minimizing distortion and complexity when interpolating

With data preprocessed and ~~sorted~~ ranked by power spectral density, the interpolation space is two-dimensional across Reynolds number (from the local inflow) and AoA. Interpolation can be done for amplitude, phase offset, and Strouhal number, for each of the lift, drag, and moment coefficient datasets. Since interpolation is done for each ~~sorted level, a limit on~~ ranked peak index, limiting the number of ~~sorted levels used~~ retained peaks can minimize the computational cost. Since the peak power spectral density tends to smoothly change with AoA, we assume that a clean dataset will inherently limit distortion from interpolation, and a fine enough grid can enable the much less costly linear interpolation methods to be used.

2.4 Combinatorial overlap reduction

Since the problem is combinatorial in nature, we address the combinations via nested for-loop logic as shown in Algorithm 1. This reduction must be done for all inflow conditions for every node in the structure, and compare against each modal frequency, harmonic, and level depth of ~~sorted~~ ranked shedding frequency. Without care in the discretization choices, this n^7 problem (assuming the same discretization for each level, for simplicity), can explode quickly.

Algorithm 1 Combinatorial Reduction

```
for each Inflow do
  for each Azimuth do
    for each Component do
      for each Node do
        Calculate Local Velocity & AoA
        Interpolate Strouhal Numbers, CL & CD Amplitudes, and Phases between Chord Reynolds and AoA
        Dimensionalize to Frequencies, Lifts, Drags
        for Each Modal Frequency do
          for each Modal Harmonic do
            for each Shedding Frequency do
              ~~Save Case if Worst & Above Filter Thresholds~~ Compute frequency-overlap difference
              Retain case if it is the highest-risk passing candidate
              Reconstruct Forcing Signals from Frequency, Lift, Drag, and Phase data
            end for
          end for
        end for
      end for
    end for
  end for
end for
```

In Algorithm 1, the frequency-overlap difference is the normalized distance between the dimensional shedding frequency and the structural frequency or harmonic being checked,

$$\Delta_f = 100 \left| \frac{f_{\text{shed}} - h f_m}{h f_m} \right|, \tag{17}$$

where f_{shed} is the scaled shedding frequency, f_m is the modal frequency, and h is the modal harmonic index. A retained highest-risk case is the passing candidate with the smallest Δ_f at the current inflow and azimuth point. The filter thresholds are user-selected limits on which candidates are considered, including the retained ranked spectral depth, the minimum force-coefficient amplitude, and any high-pass or frequency-window limits applied to remove low-energy or irrelevant spectral content.

2.5 Sensitivity to source spectral data

The overlap and load-reconstruction outputs are directly sensitive to the source spectral dataset. Since $f_{\text{shed}} = St\, V_{\text{eff}}/c_n$, an uncertainty ΔSt changes the predicted shedding frequency linearly as $\Delta f_{\text{shed}} = (V_{\text{eff}}/c_n)\Delta St$. Therefore, a Strouhal discrepancy can move overlap bands in inflow speed, AoA, and azimuth even if the structural model is unchanged. Source force-coefficient amplitude uncertainty is similarly direct: for fixed density, area, and velocity, reconstructed load amplitudes scale linearly with the stored coefficient amplitudes, while phase uncertainty primarily changes time-domain superposition and force aggregation rather than the scalar frequency-overlap metric.

This limitation is important for high-Reynolds-number datasets. For example, Ebstrup et al. (2024) report $St = 0.33$ with URANS and $St = 0.48$ with IDDES for the same wind-turbine tower-segment problem at $Re = 8.0 \times 10^6$. Such a difference would shift the corresponding VorLap shedding-frequency estimate by the same relative amount. It also indicates that URANS alone may be inadequate when the source dataset must resolve separated wake-shedding features for high-AoA or bluff-body-like flow; higher-fidelity simulations or experiments are preferable for design-quality source spectra. The present demonstration is therefore deterministic and should be read as a workflow demonstration, not as a completed probabilistic uncertainty analysis. In design use, this sensitivity can be quantified by rerunning the reduction with alternative source datasets or with explicit perturbations to Strouhal number, force-coefficient amplitude, and phase.

2.6 Signal reconstruction and load synthesis

Given the discrete amplitude spectrum A_k and phase angles ϕ_k at frequencies f_k, the time-domain coefficient $c(t)$ (e.g., C_L) can be reconstructed via the inverse Fourier synthesis (Oppenheim and Schafer, 2010):

$$c(t) = A_0 + \sum_{k=1}^{N/2} A_k \cos(2\pi f_k t + \phi_k) \tag{18}$$

where A_0 represents the mean component. This reconstruction is done for all of the forces (lift, drag, and moment). For real-valued signals, conjugate symmetry is enforced to ensure real reconstruction. Turbine-level thrust, torque, and moment time signals can be obtained by aggregating per-segment spectral contributions according to their local geometry and reference areas and integrating. These reconstructed forces represent prescribed vortex-shedding excitation for one-way coupling; motion-induced VIV forces, aerodynamic damping, and lock-in effects are not included and would require coupled fluid-structure modeling or empirical VIV models (Sarpkaya, 2004).

3 Software implementation (VorLap)

VorLap is an open-source Python framework designed to predict vortex-induced vibration risks in static or very-low-speed rotating structures using spectral flow data derived from computational fluid dynamics or experimental measurements. The software implements the algorithms discussed in the methods section and provides utilities for file IO, visualization, and a graphical user interface. While the example here is for a vertical-axis wind turbine, any application could be simulated, such as communication towers, underwater structures, horizontal-axis wind turbines, etc. The following subsections describe the core modules of the software and their roles in the overall workflow.

3.1 FileIO

The file IO module handles ingestion of structural geometry and spectral airfoil datasets from standardized file formats. Structural components are defined through CSV files containing a two-header format. The first header row specifies component-level

metadata (identifier, translation, rotation, pitch) with the corresponding values in the following row. The second header row specifies segment-wise geometry data, including spatial coordinates (x, y, z), aerodynamic parameters (chord, twist, thickness, offset), and airfoil assignment with the following rows each containing the values for an individual segment. Airfoil assignments point to an airfoil CSV file that contains the non-dimensional coordinates of the specified airfoil shape in two columns. Spectral airfoil data are loaded from HDF5 files containing three-dimensional arrays organized as [Reynolds number $\times$ AoA $\times$ Frequency] for Strouhal numbers, amplitudes, and phases of lift, drag, moment, and combined force coefficients.

The module also provides functionality for exporting computed force time series to CSV format, with structured headers indicating node positions and force components. This CSV intermediate file enables direct integration with downstream structural analysis tools for one-way coupling simulations.

3.2 Computation

The computational module implements the linear algebra transformations described in Eq. (12)–Eq. (16) to compute local AoAs and effective velocities for each structural segment across all azimuthal orientations and inflow conditions. The core computation follows the combinatorial reduction algorithm outlined in Algorithm 1, iterating through inflow speeds, azimuthal positions, components, and nodes to evaluate the complete parameter space.

The module also handles force vector transformations, rotating local lift and drag forces into the global coordinate frame using Rodrigues' rotation formula. This formulation enables computation of aggregate forces and moments at the structure level, which are accumulated across all components and segments.

Additionally, the module implements signal reconstruction functionality using the inverse Fourier transform approach described in Eq. (18). This synthesizes time-domain force signals from the interpolated spectral data, enabling generation of force time series at specified structural nodes for selected operating conditions. The reconstruction handles mean values separately from oscillatory terms and includes Nyquist frequency validation to prevent aliasing artifacts.

3.3 Visualization

The visualization module generates three-dimensional visualizations of structural geometry, including component placement, chord vectors, normal vectors, rotation axes, and inflow directions. The visualization uses Plotly for interactive 3D rendering, enabling users to inspect geometry from multiple viewpoints and validate component configurations before analysis execution.

The visualization serves both as a validation tool (ensuring geometry is correctly specified) and as a communication aid (illustrating structure configurations in presentations and documentation). The module includes fallback rendering options for headless computing environments, ensuring compatibility with automated workflows and continuous integration systems.

3.4 Graphical user interface

To improve accessibility for users without programming experience, VorLap includes a graphical user interface (GUI) implemented in Python's Tkinter framework. The interface provides an integrated workflow from data loading through results visualization, organized into two tabs:

Simulation Setup Tab: Handles parameter configuration through form-based inputs for fluid properties, inflow conditions, frequency analysis settings, and structural component loading. The interface includes real-time validation and error messaging to guide users through proper configuration. The GUI can receive input manually by editing the fields in the application or by uploading files. Uploaded files can also be modified before executed.

Plots & Outputs Tab: Provides interactive visualization of analysis results with embedded matplotlib plotting capabilities. Users can switch between different visualization modes (frequency overlap, force components, moment components) and export plots directly from the interface. The tab includes controls for adjusting plot parameters and saving results in standard image formats.

The GUI maintains full functional parity with the command-line interface, ensuring that all analyses can be reproduced through either pathway. Results are automatically saved to user-specified directories with organized folder structures for plots, time-series data, and configuration files.

4 Verification

To verify the tool is implemented without errors, we exercise the full VorLap workflow for a single blade section. The verification focused on two aspects: (1) spectral reconstruction accuracy, ensuring that frequency and amplitude content are preserved throughout the workflow, and (2) correct identification of shedding–modal frequency overlap within the discretized parameter space.

4.1 Reconstruction accuracy

The force time series from a single blade section was decomposed and reconstructed using VorLap. ~~Data from Bidadi et al. (2024) were~~ The source data for this verification are the FFA-W3-211 force histories from Bidadi et al. (2024), preprocessed as described in Sect. 2, then passed through the VorLap tool, including transformation into the frequency domain, filtering to remove uncertain low-amplitude harmonics, and reconstruction into the time domain. Figure 5 shows the reconstructed dimensional force signal compared to the reference data for the FFA-W3-211 blade with a freestream velocity of 75 ~~ms^{-1}~~m/s, a chord length of 1 m, and an AoA of -144° (216°), corresponding to reversed-flow ~~high-AoA conditions. VorLap reconstruction reproduces both the dominant frequency content and the amplitude envelope with negligible phase shift, confirming that the inverse Fourier processing and scaling methods are quantitatively accurate compared to the original data. Minor differences at lower frequencies correspond to harmonics below the user-defined amplitude threshold, which are intentionally filtered for computational efficiency. The reconstructed signalis an acceptable representation of the original data~~high-AoA conditions.

Agreement is assessed over the plotted 0–2 s window using the Pearson correlation coefficient between the demeaned original and reconstructed time histories. The correlation coefficient is $r = 0.90$, indicating that the retained reconstruction captures the dominant timing and waveform shape of this example signal. This diagnostic is not a validation of lock-in or two-way VIV response.

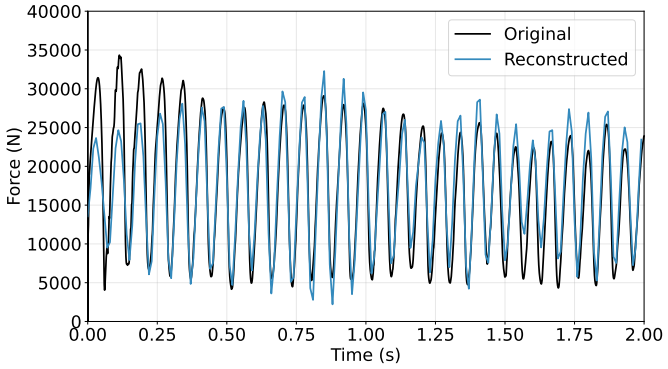


Figure 5. Original and reconstructed force time series for a single blade after VorLap processing and scaling. The ~~reconstructed signal shows good amplitude (within 5 %)~~ demeaned original and ~~phase (within 1 %) alignment~~reconstructed time histories have a Pearson correlation coefficient of $r = 0.90$ over the plotted window.

4.2 Frequency mapping verification

To confirm the frequency scaling methods, the scaled spectrum was compared against a modal frequency of 15 Hz, chosen intentionally to match one of the dominant frequencies present in the airfoil force data. This verification was done for a variety of inflow angles, speeds, and high-pass filtering. The heatmap shown in Figure 6 gives the results from VorLap, verifying that the dimensionalization via Strouhal scaling correctly adjusts shedding frequencies with changing inflow velocity. The peak overlap identified by VorLap occurred at the expected angle and velocity combinations, consistent with the known dominant shedding modes near 15 Hz for the 216° AoA case. This verification demonstrates correct implementation of frequency scaling and interpolation and gives us greater confidence as we move to the full structure demonstration.

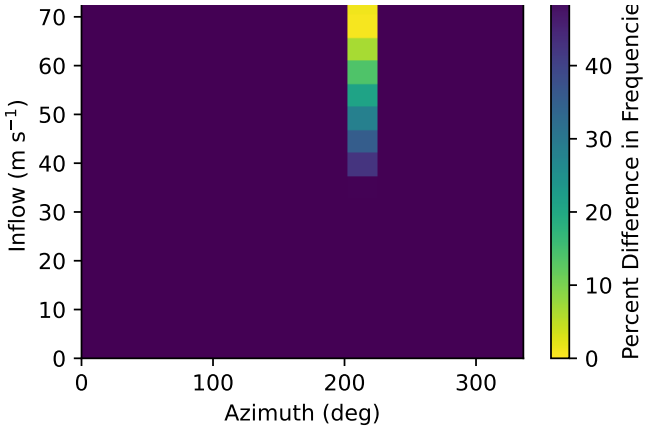


Figure 6. Heatmap showing the worst case overlap of a 15 Hz modal frequency and scaled shed frequencies, including high-pass filtering. The expected overlap at 216° AoA is highlighted.

5 Demonstration with example structure

The motivation in Sect. 1.1 showed a simplified approach to identify that there was a potential for vortex-induced vibration onset during parked conditions for the reference H-VAWT in Moore et al. (2024) (geometry shown in Fig. 4). In this section, we exercise the VorLap tool to refine the identification of potential areas of overlap and then demonstrate sample forcing signal reconstruction.

It is important to reiterate that different environmental conditions, airfoils, and fluid scaling (Reynolds number), may necessitate using vortex shedding datasets that are for the application. Therefore, for this paper, we present an architecture and method for how to navigate this highly dimensional problem and properly scale both the frequency and forces, but we recommend using datasets that appropriately match the application space.

5.1 Model setup

For this example demonstration, the turbine analysis was done with the configuration shown in Table 1 and using the ~~example computational fluid dynamics (CFD) dataset previously discussed.~~preliminary VorLap NACA 0018 CFD force-history dataset described in Sect. 2. The demonstration is intended to simulate a wide variety of possible vortex shedding frequency overlap where shedding may occur (a distributed wind turbine during normal parked conditions). We do not simulate high wind speed because it is anticipated that the turbulence intensity will dominate the loading and likely disrupt vortex shedding (Blackburn and Melbourne, 1996).

Table 1. Reference turbine and simulation definition.

Name	Value
Diameter	10.5 m
Blade & Strut Chord	0.5 m
Blade Height	10.54 m
Blade Airfoil	NACA 0018
Struts per Blade	2
Strut Angle	30°
Wind Vector	(1,0,0)
Rotation Vector	(0,0,1)
Rotation Axis Offset	(0,0,0)
Fluid Density	1.225 ~~kgm^{-3}~~ kg/m^3
Fluid Dynamic Viscosity	1.81E-5 ~~Pa-s~~ Pa s
Azimuth Range	0:5:120°
Inflow Velocity Range	1–16 m/s in 1 ~~:1:16 ms^{-1}~~ m/s increments
Number of Modal Harmonics	1
Sorted Frequency Comparison Depth	10
Amplitude Coefficient Minimum Cutoff	0.5

The azimuth range was sampled in 5° increments and restricted to 120° due to symmetry (noted below). The turbine rotates about a vertical axis, so either wind speed or parked azimuth could change the relative azimuth angle. Since the tool was designed to be application agnostic, the frame of reference for azimuth follows standard mathematical notations (0° is at the east position). To align with vertical-axis wind turbine notation (0° at the north position), the input geometry was simply defined as rotated by 90°.

Using the structural definition and solver in (Moore et al., 2024), the first natural or modal frequencies for the structure are 2.711, 6.021, 7.151, 7.689, 7.863, and 11.615 Hz. The shapes are visually depicted in Fig. 7. Of note is that the third mode is a series of combinatorial variations of the three blades bending in and out of sync with one another, spanning 7.151, 7.689, and 7.863 Hz. These natural frequencies, and their respective harmonics, are what we compare the shedding frequencies to.

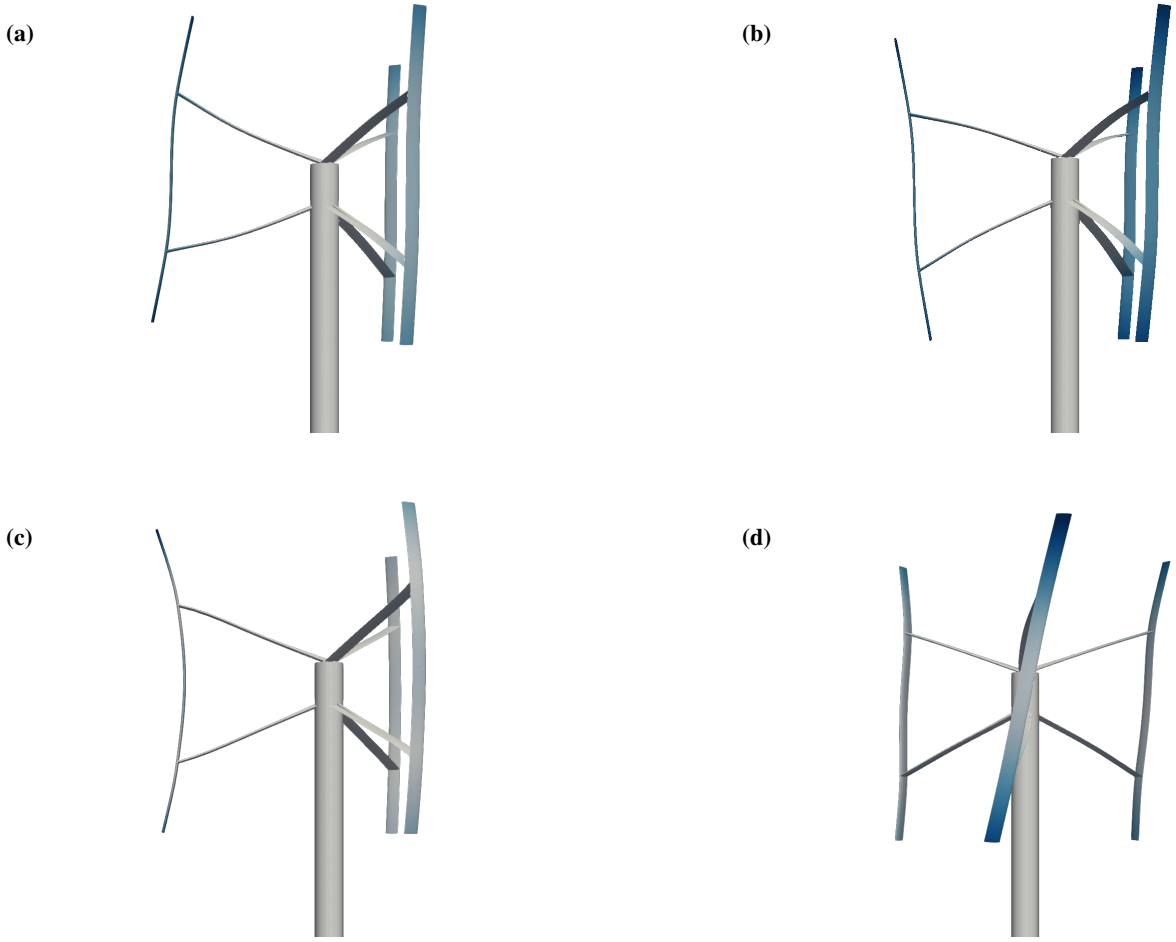


Figure 7. Mode shapes and frequencies for the reference turbine, using the structural definition and solver in Moore et al. (2024). First mode (a), associated with 2.711 Hz. Second mode (b), associated with 6.021 Hz. Third mode (c), associated with the family of 7.151, 7.689, and 7.863 Hz (different combinations of blade bending in or out of sync). Fourth mode (d), associated with 11.615 Hz.

5.2 Frequency overlap examples and discussion

While the example structure may experience any direction of inflow velocity during parked conditions due to flow direction change, the turbine may tend to stop at zero-torque azimuthal positions across the full 360° azimuth range more frequently. However, due to the three blade and arm sets being fully symmetrical, we can focus on a range up to 120° azimuth.

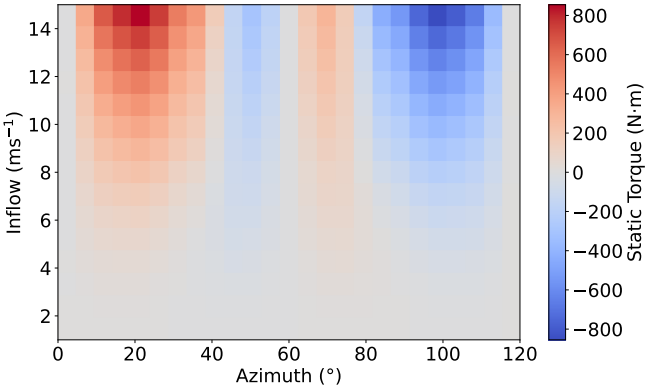


Figure 8. Static torque for the reference turbine about the axis of rotation showing low torque bands around 0°, 60°, and 120°, as well as 45° and 75° to a lesser extent.

Figure 8 shows the static torque for the reference turbine about the axis of rotation for azimuths of 0° to 120°. Low torque positions include 0°, 60°, and 120°, and to a lesser extent 45° and 75°. All positions need to be considered, but these positions provide possible higher probability parked configurations for this particular application.

365

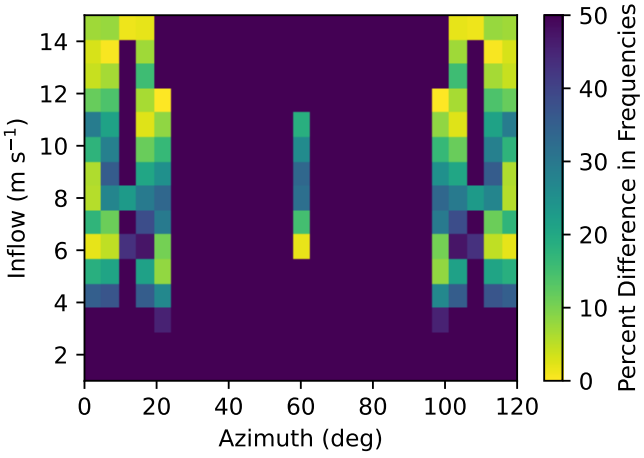


Figure 9. Heatmap showing the percent difference between the reduced combinatorial set, including filtering thresholds, of modal frequencies and scaled shed frequencies.

With these higher-probability positions in mind, we now consider the heatmap in Fig. 9 showing the case with the highest frequency overlap. The worst-case amplitude and frequency overlap scenario is shown because the coefficient filter is set high enough that only the highest-amplitude cases are being considered in the combinatorial reduction. For designers using this tool, it is recommended that they consider multiple different filtering levels to understand problem areas for their specific designs and

370 establish logical thresholds based on structural damping, ~~etc.~~ resonance bandwidth, and acceptable screening margin. As in the verification case, the heatmap reports the minimum percent difference across multiple harmonics and ranked shedding peaks,

so a close frequency match can persist at higher inflow velocities even when the forcing amplitude is small. This behavior reflects the screening metric rather than sustained lock-in.

The first observation from this demonstration is that the high-level analysis done at the beginning of the paper appears to have been correct, but that a high degree of overlap risk (the bright yellow areas) is isolated to specific conditions. The second observation is that the results appear to be highly symmetric about 60° azimuth. This symmetry would appear to be in large part to the thin, non-cambered profile of the NACA 0018 acting similar to a flat plate during high AoAs. Referring back to Fig. 3, the variations in shedding frequency appear to become non-symmetric between forward and reversed flow only at lower relative AoAs. However, for those conditions, the shedding amplitude drops off sharply and is filtered out. For a thicker or cambered airfoil, these trends would likely be different, but for this study with a high degree of symmetry due to the airfoil geometry, we may further refine the focus to between 0° and 60°. The present overlap metric does not account for structural damping or resonance bandwidth, so percent frequency difference should be interpreted as a screening indicator rather than a lock-in criterion; designers should compare these differences against their modal damping bandwidth and VIV lock-in guidance (Sarpkaya, 2004).

Focusing on azimuth angles between 0° and 60°, Table 2 shows a few example summaries of high-risk overlap conditions and where they occur. With the filtering so selective, the cases highlighted are limited to the peak amplitude of the input data, and a designer would need to determine if this threshold is appropriate for the structure. The trends shown tend to favor higher AoAs until flow reversal effectively creates a shallow AoA again. Also, for this case, the higher-frequency modes tend to be overlapped only with higher velocity flow, so they may not be seen often for this type of structure except during certain maintenance conditions. For example, if a turbine was parked for maintenance and the wind speed increased above the normal operation cut-in, then a higher-frequency mode might become excited.

Table 2. Sample high-risk overlap summaries for the first modal harmonic. Note the fourth mode was dominated by overlap with the other modes for this case.

Mode	Harmonic	Azimuth	Inflow	% Difference	Location	AoA	Chord Reynolds
1	1	0°	6 ~~ms^{-1}~~ m/s	1.9 %	Blade 3	120°	203k
1	1	60°	6 ~~ms^{-1}~~ m/s	1.6 %	Blade 3	60°	203k
1	1	0°	8 ~~ms^{-1}~~ m/s	5.6 %	Arm 2	140°	179k
2	1	20°	12 ~~ms^{-1}~~ m/s	0.13 %	Blade 2	-140°	406k
2	1	5°	15 ~~ms^{-1}~~ m/s	7.7 %	Blade 3	115°	507k
2	1	60°	11 ~~ms^{-1}~~ m/s	18.4 %	Blade 3	60°	372k
3	1	0°	15 ~~ms^{-1}~~ m/s	7.1 %	Blade 3	120°	507k
3	1	10°	15 ~~ms^{-1}~~ m/s	1.3 %	Blade 2	-130°	507k
3	1	0°	15 ~~ms^{-1}~~ m/s	1.8 %	Blade 3	-135°	507k

Also of note is that while the blades tend to dominate the samples chosen, other components can begin to overlap. In the Arm 2 overlap sample case, the local velocity that the shedding frequency is scaled with is in the local blade frame of reference (note Sect. 2.2), which, with a skew angle, decreases the inflow and in turn the shed frequency. This factor changes the range

of predicted frequencies being shed, leading to possible overlap. For high skew angles, this assumption may not hold, as shed vortices may tend to combine, changing the shed frequency (Zhang et al., 2023).

5.3 Signal reconstruction and discussion

For this demonstration, we choose the second-line case in Table 2. This condition has shedding alignment coming from the third blade, and since the blade is uniform and straight (as opposed to a different design with variable chord, twist, shape, etc.), the reconstructed signal for all of the nodes along the blade are the same, so we choose the second node. Now, as discussed in Sect. 2.6, we use all the frequency and phase content for both the lift and drag at this interpolated AoA and Reynolds number. We recall that the data were scaled to the size and flow conditions for frequency via the Strouhal scaling, and the forces were scaled through lift and drag coefficient scaling.

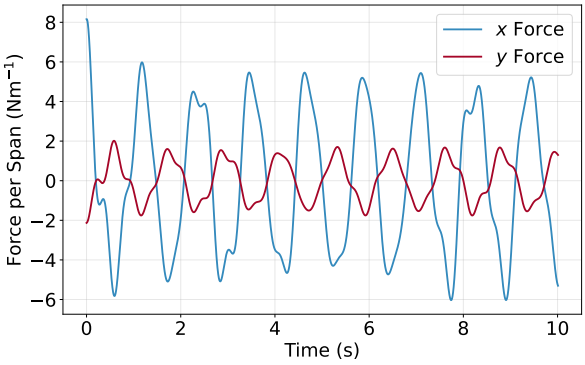


Figure 10. Sample reconstructed force time signals for Blade 3, Node 2 at the 60°, 6 ~~ms^{-1}~~ m/s turbine parked condition.

Figure 10 shows the sample reconstructed force time signals for Blade 3, Node 2 at the 60°, 6 ~~ms^{-1}~~ m/s turbine parked condition in the turbine global x and y directions. Using this same method for all defined nodes across all components with their respective conditions, a full set of structural loads can be created and can be used in one-way coupling with structural modeling software. These capabilities are automated in the VorLap tool, enabling designers to conduct further structural analyses. Additionally, a designer could iteratively export loads for differing inflow velocities and angles and combine them to create a loading profile representative of long-term parked conditions.

6 Conclusions

This work presents a reproducible, open-source framework for evaluating vortex-induced vibration onset using spectral flow data, enabling systematic identification of overlap between vortex shedding frequencies and structural natural frequencies. The VorLap method and accompanying software establish a consistent means of scaling and interpolating high-dimensional aerodynamic data spanning Reynolds number, AoA, and geometry to arbitrary multi-body structures. By combining spectral

decomposition, linear algebraic transformations, and combinatorial reduction, the workflow bridges the gap between fundamental unsteady flow data and engineering design application. For a broad variety of structures, such as radio towers, underwater structures, horizontal-axis wind turbines, vertical-axis wind turbines, and others, designers can utilize VorLap to quickly identify, avoid, and include vortex-induced vibration considerations in their design processes.

Verification against published CFD datasets and reconstructed time-domain signals demonstrated that the approach preserves ~~both frequency and amplitude fidelity~~ dominant frequency and phase information through the complete data pipeline, while amplitude agreement remains sensitive to filtering, retained spectral depth, and source-data quality. Further verification and validation would be ideal in future work. Application to a reference vertical-axis wind turbine illustrated how specific vortex shedding frequencies can align with modal responses under specific parked conditions, corroborating the analytical intuition outlined in the motivation section.

The results suggest that spectral lift and drag datasets, when treated through non-dimensional scaling and organized interpolation, can support early-stage design screening for the risk of vortex-induced vibration onset. However, the resulting overlap bands and reconstructed loads inherit uncertainty from the source spectral dataset, so design use should include alternate datasets or explicit perturbations in Strouhal number, amplitude, and phase. Also, the open architecture of VorLap facilitates integration with existing structural solvers for one-way coupled load reconstruction or reduced-order modeling. Future work is anticipated to result in a high-quality CFD dataset and improvements to skew corrections.

Code and data availability. The VorLap code and example datasets can be found at https://github.com/sandialabs/VorLap. The preliminary NACA 0018 CFD example dataset, the FFA-W3-211 processed verification dataset, and the demonstration inputs are included with the repository test and example assets.

Author contributions. **Conceptualization:** KRM; **Methodology:** KRM, KLB; **Software:** KRM, KLB; **Validation:** HKR, KRM; **Visualization:** KRM, KLB, HKR; **Writing, original draft:** KRM; **Writing, review & editing:** KRM, HKR, KLB; **Supervision/Project administration/Funding acquisition:** BJS

Competing interests. The authors declare that they have no conflict of interest.

Disclaimer. Sandia National Laboratories is a multi-mission laboratory managed and operated by National Technology & Engineering Solutions of Sandia, LLC (NTESS), a wholly owned subsidiary of Honeywell International Inc., for the U.S. Department of Energy's National Nuclear Security Administration (DOE/NNSA) under contract DE-NA0003525. This written work is authored by an employee of NTESS. The employee, not NTESS, owns the right, title and interest in and to the written work and is responsible for its contents. Any subjective views or opinions that might be expressed in the written work do not necessarily represent the views of the U.S. Government. The

445 publisher acknowledges that the U.S. Government retains a non-exclusive, paid-up, irrevocable, world-wide license to publish or reproduce the published form of this written work or allow others to do so, for U.S. Government purposes. The DOE will provide public access to results of federally sponsored research in accordance with the DOE Public Access Plan.

This work was authored in part by the National Laboratory of the Rockies for the U.S. Department of Energy (DOE), operated under Contract No. DE-AC36-08GO28308. Funding provided by U.S. Department of Energy Office of Energy Efficiency and Renewable Energy Wind
450 Energy Technologies Office. The views expressed in the article do not necessarily represent the views of the DOE or the U.S. Government. The U.S. Government retains and the publisher, by accepting the article for publication, acknowledges that the U.S. Government retains a nonexclusive, paid-up, irrevocable, worldwide license to publish or reproduce the published form of this work, or allow others to do so, for U.S. Government purposes.

Acknowledgements. This work has been funded by the United States Department of Energy (DOE) Wind Energy Technologies Office under
455 the Distributed Wind Aeroelastic Modeling (dWAM) project. AI tools were used in the conceptualization and rough drafting phases of the method, software, and paper. However, due to the high AI error rate, all AI generated content was manually rewritten or extensively reviewed and modified to produce draft and final products.

References

Benner, B. M., Carlson, D. W., Seyed-Aghazadeh, B., and Modarres-Sadeghi, Y.: Vortex-Induced Vibration of symmetric airfoils used in Vertical-Axis Wind Turbines, Journal of Fluids and Structures, 91, 102 577, https://doi.org/10.1016/j.jfluidstructs.2019.01.018, 2019.

Bidadi, S., Vijayakumar, G., Deskos, G., and Sprague, M. ~~A.: Three-dimensional aerodynamics and vortex-shedding of wind turbine airfoils over 360-degree angles of attack~~: Three-Dimensional Aerodynamics and Vortex-Shedding Characteristics of Wind Turbine Airfoils over 360-Degree Angles of Attack, Energies, 17, 4328, https://doi.org/10.3390/en17174328, 2024.

Blackburn, H. M. and Melbourne, W. H.: The effect of free-stream turbulence on sectional lift forces on a circular cylinder, Journal of Fluid Mechanics, 306, ~~267–292~~267–292, https://doi.org/10.1017/S0022112096001309, 1996.

Chen, J. M. and Fang, Y. ~~C~~ C.: Strouhal numbers of inclined flat plates, Journal of Wind Engineering and Industrial Aerodynamics, 61, 99–112, https://doi.org/10.1016/0167-6105(96)00044-X, 1996.

Ebstrup, K., Nørmark Sørensen, N. N., Bertagnolio, F., Grindersley, C., and Horcas, S. G.: Numerical investigation of vortex-induced forces on a wind turbine tower segment at very high Reynolds numbers, Journal of Physics: Conference Series, 2767, 022 048, https://doi.org/10.1088/1742-6596/2767/2/022048, 2024.

Fernandez-Aldama, R., ~~Martínez-Tossas, L.~~Papadakis, G., Lopez-Garcia, O., Avila-Sanchez, S., Riziotis, V. A., ~~Sarlak, H~~Cuerva-Tejero, A., and ~~Breton, S. P.: Vortex-shedding~~ Gallego-Castillo, C.: Characterization of vortex-shedding regimes and lock-in ~~for~~ response of a wind turbine airfoil ~~at 90° incidence~~with two high-fidelity simulation approaches, Wind Energy Science, 10, 17–39, https://doi.org/10.5194/wes-10-17-2025, 2025.

Grindersley, C., ~~Zahle, F., Barlas, E., and Madsen, H. A.: Multiple stable~~ Nørmark Sørensen, N., Pirrung, G. R., and González Horcas, S.: Multiple limit cycle amplitudes in high-fidelity predictions of standstill wind turbine blade vibrations~~due to vortex-induced excitation~~, Wind Energy Science, 7, 2201–2213, https://doi.org/10.5194/wes-7-2201-2022, 2022.

Grindersley, C.~~et al.~~, Houtin-Mongrolle, F., Nørmark Sørensen, N., Pirrung, G. R., Jacobs, P., Ahmed, A., and Duboc, B.: Forced-motion simulations of vortex-induced vibrations ~~on~~ of wind turbine blades – a study of sensitivities, Wind Energy Science, 8, 1625–1638, https://doi.org/10.5194/wes-8-1625-2023, 2023.

Moore, K. R., Brownstein, I. D., and Ross, H. K.: Critical design load case fatigue and ultimate failure simulation for a 10-m H-type vertical-axis wind turbine, Journal of Physics: Conference Series, 2767, 072 025, https://doi.org/10.1088/1742-6596/2767/7/072025, 2024.

Oppenheim, A. V. and Schafer, R. W.: Discrete-Time Signal Processing, Pearson, Upper Saddle River, ~~NJ, 3~~ New Jersey, 3rd edn., ISBN 978-0131988422 , 2010.

Roshko, A.: Experiments on the flow past a circular cylinder at very high Reynolds number, Journal of Fluid Mechanics, 10, 345–356, https://doi.org/10.1017/S0022112061000950, 1961.

Sakib, M. S. and Griffith, D. T.: Parked and operating load analysis in the aerodynamic design of multi-megawatt-scale floating vertical-axis wind turbines, Wind Energy Science, 7, 677–696, https://doi.org/10.5194/wes-7-677-2022, 2022.

Sandia National Laboratories: VorLap: Generalized Vortex Overlap Fluid Structure Interaction Prediction Code, https://github.com/sandialabs/VorLap, gitHub repository, accessed 29 June 2026, 2026.

Sarpkaya, T.: A critical review of the intrinsic nature of vortex-induced vibrations, Journal of Fluids and Structures, 19, 389–447, https://doi.org/10.1016/j.jfluidstructs.2004.02.005, 2004.

Schewe, G.: On the force fluctuations acting on a circular cylinder in crossflow from subcritical up to transcritical Reynolds numbers, Journal of Fluid Mechanics, 133, 265–285, https://doi.org/10.1017/S0022112083001913, 1983.

Sheldahl, R. E. and Klimas, P. C.: Aerodynamic characteristics of seven symmetrical airfoil sections through 180-degree angle of attack for use in aerodynamic analysis of vertical axis wind turbines, Tech. Rep. SAND-80-2114 , Sandia National Laboratories, https://doi.org/10.2172/6548367, 1981.

Swalwell, K., Sheridan, J., and Melbourne, W. H.: Frequency analysis of surface pressures on an airfoil after stall: Frequency Analysis of Surface Pressures on an Airfoil After Stall, in: 21st AIAA Applied Aerodynamics Conference, pp. 2003–3425, https://doi.org/10.2514/6.2003-3416, 2003.

VimalKumar, S., Korkut, E., Barlas, E., and Zahle, FDe Tavernier, D., von Terzi, D., Belloli, M., and Viré, A.: Force-partitioning analysis of vortex-induced vibrations of wind turbine tower sections, Wind Energy Science, 9, 1967–1983, https://doi.org/10.5194/wes-9-1967-2024, 2024.

Zhang, K., Bao, Y., Han, Z., and Zhou, D.: End boundary effects on wakes dynamics of inclined circular cylinders, Ocean Engineering, 269, 113 543, https://doi.org/10.1016/j.oceaneng.2022.113543, 2023.